

Ir-catalysed Nitrous oxide (N₂O) decomposition: Effect of Ir particle size and metal-support interactions

I.V. Yentekakis¹, G. Goula¹, S. Kampouri¹, I. Betsi-Argyropoulou¹, P. Panagiotopoulou¹, M.J. Taylor², G. Kyriakou², R.M. Lambert³

¹ School of Environmental Engineering, Technical University of Crete, 73100- Chania, Crete, Greece.

² European Bioenergy Research Institute, Chemical Eng. & Appl. Chem., Aston University, Aston Triangle, Birmingham, B4 7ET, UK.

³ Chemistry Department, Cambridge University, UK and Instituto de Ciencia de Materiales de Sevilla (CSIC), Americo Vespucio 49, 41092 Seville, Spain.

Abstract

The effect of the morphology of Ir particles supported on γ -Al₂O₃, 8mol% Y₂O₃-stabilized ZrO₂ (YSZ), 10mol% Gd₂O₃-doped CeO₂ (GDC) and 80wt% Al₂O₃-10wt% CeO₂-10wt% ZrO₂ (ACZ) on their stability on oxidative conditions, the associated metal-support interactions and activity for catalytic decomposition of N₂O has been studied. Supports with intermediate or high oxygen ion lability (GDC and ACZ) effectively stabilized Ir nanoparticles against sintering, in striking contrast to supports offering negligible or low oxygen ion lability (γ -Al₂O₃ and YSZ). Turnover frequency studies using size-controlled Ir particles showed strong structure sensitivity, de-N₂O catalysis being favoured on large catalyst particles. Although metallic Ir showed some de-N₂O activity, IrO₂ was more active, possibly present as a superficial overlayer on the iridium particles under reaction conditions. Support-induced turnover rate modifications, resulted from an effective double layer [O^{δ-} - δ⁺](Ir) on the surface of iridium nanoparticles, via O²⁻ backspillover from the support, were significant in the case of GDC and ACZ.

Keywords: Iridium; Nitrous oxide decomposition; Thermal aging; Particle growth; nanoparticles sintering; Ostwald Ripening; Ionic conductor; oxygen ion lability; Oxygen storage capacity; Turnover frequency; Alumina; Ceria; Zirconia

1. Introduction

N₂O is a powerful greenhouse gas (global warming potential ~300) and also the dominant ozone-depleting gas of the twenty-first century [1, 2]. Stationary or mobile combustion sources and certain chemical processes, are the main sources of anthropogenic N₂O emissions, whose abatement is therefore of global importance. In this context, the catalytic reduction of N₂O to N₂ is a most promising approach [3].

A wide range of materials have been investigated as catalysts, including noble metals, transition metals, mixed oxides, perovskites and zeolites [4-8]. Among them, noble metals (NMs) exhibit good activity at intermediate temperatures so despite their high cost they are promising candidates for practical implementation [3,4]. Rh exhibits the best catalytic activity, although Ru and Ir, significantly cheaper, are almost as good [7,9]. However, a drawback of both Ir and Ru nanoparticle catalysts is their well known inferior thermal stability compared to Rh and Pt [10].

We have recently shown that the thermal sintering characteristics of Ir are strongly correlated with the lability of lattice oxygen in the oxide supports [11] and that metal-support interactions between Ir and oxide supports having high oxygen ion lability can strongly stabilize Ir nanoparticles at high temperatures under oxidizing conditions. It is well known that such supports can also strongly modify the electronic state of the active phase interfaced with them, and, depending on the electrophilic or –phobic character of the reactants, promote or inhibit the catalytic chemistry [12, 13]. Here we clarify the influence of these phenomena on the direct decomposition of N₂O by means of well characterized supported Ir catalysts whose particle size and morphology were controlled by aging. Specifically, we extend the general applicability of our model for the inhibition of sintering to include the important case of Ostwald Ripening. Furthermore, we report the first observation of a counter-clockwise hysteresis phenomenon in light-off curves of Ir-catalysed N₂O decomposition and discuss their origin.

2. Experimental

2.1. Materials preparation

The support materials were γ -Al₂O₃ (Engelhard), 8 mol% yttria stabilized zirconia, YSZ (Zirconia sales, UK Ltd.), 10 mol% gadolinia doped ceria, GDC (Anan Kasei Co, Ltd.) and laboratory made by co-precipitation ACZ (80wt% Al₂O₃-10wt% CeO₂-10wt% ZrO₂ mixed oxide). All were pre-treated in air at 800°C for 2h. Ir-dispersed catalysts, Ir/ γ -Al₂O₃, Ir/YSZ, Ir/GDC, and Ir/ACZ, were prepared by wet impregnation of the supports at 75°C in a solution of IrCl₃·H₂O (Abcr GmbH & Co.KG)

followed by reduction in H₂/He flow to yield 1.0 wt% nominal Ir loading. The actual metal loading was determined by induced coupled plasma optical emission spectroscopy (ICP-OES). After water evaporation, suspensions were dried at 110°C for 12 h and the resulting powders heated at 400°C for 2h under 50% H₂/He flow and then at 850°C for 1h under 1% H₂/He flow (hereafter denoted as *fresh* catalysts). This produced a very narrow Ir particle size distribution (1-2 nm), unlike other methods in which an oxidation step (instead of a reduction) is used at this stage leading to a broad Ir size distribution (from ~1 to > 150 nm) [9,14]. In addition, this prolonged H₂ treatment allows the effective removal of residual chlorine resulting from the IrCl₃ precursor used. In order to study the susceptibility of our catalysts toward sintering and the consequent influence on their de-N₂O activity, pre-aged counterparts of the four catalysts were prepared from the fresh samples using the following protocol: two consecutive cycles of 1 h oxidation (20%O₂/He, 50 cm³min⁻¹, 750°C) followed by 0.5h reduction (2%H₂/He, 50 cm³min⁻¹, 750°C)” (hereafter referred to as *aged* catalysts).

2.2. Materials characterization and catalytic evaluation

N₂ adsorption-desorption (BET), isothermal hydrogen chemisorption (H₂-chem.), hydrogen Temperature-Programmed Reduction (H₂-TPR), Inductively Coupled Plasma Optical Emission Spectroscopy (ICP-OES), High Resolution Transmission Electron Microscopy (HRTEM) and Powder X-ray Diffraction (PXRD) were used to determine the textural, structural and morphological characteristics of the fresh and aged catalysts. BET surface areas (S_{BET}) and total pore volumes of degassed samples were obtained using a Nova 2200e Quantachrome with N₂ as adsorbate. Isothermal H₂ pulse-chemisorption measurements using H₂ pre-reduced samples were acquired with a Quantachrome/ChemBet Pulsar TPR/TPD chemisorption analyzer with simultaneous use of a TCD and an Omnistar/Pfeiffer Vacuum mass spectrometer. To avoid H₂ spillover effects the chemisorption experiments were conducted at 0°C. This allowed determination of the H/Ir ratio (i.e. iridium dispersion) and the mean Ir crystallite size. Oxygen storage capacities (OSC) of the oxygen-saturated supports were determined by means of H₂-TPR measurements using the same apparatus. Iridium contents were determined by ICP-OES (Thermo Scientific iCAP 7400 duo) after microwave digestion (CEM–MARS microwave reactor) of the samples in 5 ml 70% HNO₃ and 100 mg NH₄F (Sigma Aldrich, ≥98.0%) at 190°C followed by dilution in 10% aqueous HNO₃. Powder X-ray diffraction (PXRD) was performed on a Bruker D8 Advance diffractometer using monochromated Cu K_{α1} radiation (λ = 0.1542 nm). Electron microscopy experiments were performed with a JEOL 2100F High Resolution Transmission Electron Microscope (HRTEM), operated at 200 kV. Samples were

dispersed in methanol and deposited on 300-mesh carbon supported copper grids and dried under ambient conditions.

Catalytic testing and stability measurements were carried out in a continuous flow apparatus equipped with a single-pass, tubular, quartz, fixed-bed reactor operated in both differential and integral modes. Catalyst bed temperature was measured via a centrally located K-type thermocouple. Reactor inlet and outlet gases were analysed by on-line gas chromatography (Shimatzu GC-2014, TC detector, He carrier, MS 5A and HayeSep D columns). Nitrogen and oxygen mass balances on the basis of the reactor inlet N₂O concentration and the outlet N₂ and O₂ concentrations measured by on-line GC were found to be better than 98% in all cases. The feed composition was always 1000 ppm(v) N₂O balanced with He. Evaluation of catalyst performance as a function of temperature (*light-off* profiles) was carried out at 300-550°C with a total feed flow rate of F_i=150 cm³min⁻¹; differential reactor operation for intrinsic activity evaluation (i.e., turnover frequency), was performed maintaining N₂O conversion below ~15%.

3. RESULTS AND DISCUSSION

3.1. Textural, structural and other characteristics of the materials

The OSCs of the four supports and associated characteristics, are shown in Table 1.

Table 1: Total oxygen storage capacity (OSC) of the supports and their characteristics

Support	Total OSC ($\mu\text{mol O}_2/\text{g}$)	Temperature of redox properties activation ($^{\circ}\text{C}$)	Low temperature peak ($^{\circ}\text{C}$)	High temperature peak ($^{\circ}\text{C}$)
$\gamma\text{-Al}_2\text{O}_3$	0.0	-	-	-
YSZ	5.7	425	505	-
ACZ	116.0	300	630 (big)	900 (small)
GDC	185.5	500	630 (small)	900 (big)

In accord with the literature [15, 16], $\gamma\text{-Al}_2\text{O}_3$ and YSZ showed negligible and very small OSC of 0 and 5.7, respectively, whereas ACZ and GDC exhibited substantial OSC of 116 and 185.5 $\mu\text{mol O}_2/\text{g}$, respectively (Table 1). The higher capacity of GDC was expected as it contains a higher proportion of CeO₂ (~90%) than does ACZ (~10%). Both GDC and ACZ showed two broad peaks in their H₂-TPR profiles [17]. For ACZ these peaks are located at ~630°C (larger) and ~900°C (smaller);

For GDC the peaks appeared at the same temperatures but the high temperature peak was much larger than the low temperature one (Table 1). Note that the redox (H_2 -consumption) behavior of ACZ was activated at a significantly lower temperature ($\sim 300^\circ C$) than for GDC ($\sim 500^\circ C$). The low temperature peak of CeO_2 -based materials is attributed to the reduction of small surface particles whereas the high temperature peak is assigned to the reduction of bulk CeO_2 [17]. We thus conclude that in the ACZ composite the CeO_2 - ZrO_2 species are preferentially located at the surface of the γ - Al_2O_3 particles as a capping layer. As we shall see, both the magnitude of the OSC *and* its detailed characteristics have important implications for N_2O decomposition catalysed by Ir particles supported on ACZ and GDC.

Textural characteristics of the supporting materials and of the fresh and aged catalysts are summarized in Table 2. Only marginal differences in the total surface areas, S_{BET} , resulted from incorporation of Ir onto the supports. ACZ was an exception; the pronounced sensitivity of its surface area to high temperature treatments is well known [16, 18]. The supports span a wide range of S_{BET} values, with YSZ lowest (ca. $5\text{ m}^2/\text{g}$) and γ - Al_2O_3 highest ($178\text{ m}^2/\text{g}$). High temperature aging resulted in only marginal changes (Table 2).

Table 2. Textural properties of the supports and fresh and aged catalysts

Catalyst	wt%Ir ^a	S_{BET} ($\text{m}^2\text{ g}^{-1}$)			Total pore volume ($\text{cm}^3\text{ g}^{-1}$)			Average pore size diameter (nm)		
		support	fresh cat.	aged cat.	support	fresh cat.	aged cat.	support	fresh cat.	aged cat.
Ir/ γ - Al_2O_3	0.7	178	159	140	0.600	0.550	0.310	13.5	13.9	8.9
Ir/YSZ	0.7	5	4	4	0.009	0.008	0.009	6.7	8.2	7.8
Ir/GDC	0.4	10	10	10	0.026	0.036	0.016	9.9	14.1	6.1
Ir/ACZ	0.4	149	73	64	0.290	0.216	0.203	7.9	11.9	12.7

^a Iridium content determined by ICP-OES.

Table 3 summarizes the H_2 -chemisorption, PXRD and HRTEM data. All the fresh catalysts exhibited small Ir particles ($\sim 1 - 2\text{ nm}$), regardless of the nature and surface area of the support, despite the large variation in the latter (Table 3). This most probably results from the low Ir loading and the reduction used in the preparation protocol. In contrast, the aged samples showed a very strong dependence of Ir catalyst particle size on the identity of the support. Ir/ γ - Al_2O_3 underwent extensive growth of the Ir particles from 0.8 to 28.8 nm; Ir/YSZ significantly less ($2.2 \rightarrow 22.6\text{ nm}$); *GDC and ACZ were almost unaffected* (1.5 to 1.8 and 1.8 to 1.6, respectively).

Table 3. Ir particle size characteristics of the fresh and aged catalysts

Catalyst	H ₂ -uptake (m ³ g ⁻¹)		Mean Ir particle size (nm)			Dispersion (H/Ir)	
	<i>fresh cat.</i>	<i>aged cat.</i>	<i>H₂-Chem</i> <i>fresh/aged</i>	<i>PXRD</i> <i>fresh/aged</i>	<i>HRTEM</i> <i>Fresh/aged</i>	<i>fresh cat.</i>	<i>aged cat.</i>
Ir/γ-Al ₂ O ₃	0.392	0.011	0.8/28.8	n.a./28.4	1.2 ± 0.4 / 14.5 ± 6.5 (max. 150)	0.88	0.03
Ir/YSZ	0.145	0.014	2.2/22.6	n.a./28.7	1.2 ± 0.4 / 10.5 ± 5.5 (max. 34)	0.33	0.03
Ir/GDC	0.121	0.103	1.5/1.8	n.a./n.a.	1.7 ± 0.5 / 2.0 ± 1.0	0.48	0.41
Ir/ACZ	0.103	0.114	1.8/1.6	n.a./n.a.	1.6 ± 0.5 / 1.9 ± 0.4	0.41	0.45

The particle sizes derived from H₂-chemisorption were very close to those estimated from PXRD data Scherrer analysis, although in the case of very small particles Ir were not detectable by PXRD. On the other hand, pre- and post aging particle sizes obtained from HRTEM are in broad agreement with those obtained from the other two methods; the apparent discrepancy in the cases of aged Ir/γ-Al₂O₃ and Ir/YSZ is due the presence of individual particles together with large aggregates of particles with maximum sizes of about 150 and 34 nm, respectively (for Ir/γ-Al₂O₃ see Figs. 1a, b). Similarly, in aged Ir/YSZ, most of the Ir particles had undergone significant changes in shape and substantial increases in size (10.5 nm) compared to the fresh sample. *In contrast, the nanoparticles supported on the aged Ir/GDC and aged Ir/ACZ retained their original small size and uniform spatial distribution.*

The susceptibility to sintering of Ir particles on γ-Al₂O₃ under oxidizing conditions due to the high volatility of IrO₂, is well known [10]. In contrast, metallic Ir particles are very stable during high temperature treatments in reducing atmospheres [10, 11].

Figure 1. HRTEM dark field images of the fresh and aged Ir/γ-Al₂O₃ samples.

The key point arising from our results is that the strong resistance to sintering in an oxidising environment of Ir particles on supports with high oxygen ion lability (GDC and ACZ) is dramatically different from their vulnerable behaviour on supports with negligible or low oxygen ion lability (γ-Al₂O₃ and YSZ). This is clearly demonstrated in Figure 2, which depicts the percentage of sintering

(i.e., % growth of Ir particles = $100 \times (\text{PS}_{\text{aged}} - \text{PS}_{\text{fresh}}) / \text{PS}_{\text{fresh}}$; PS: particle size) resulting from oxidative aging of the catalysts versus the OSC of the supports. Clearly, there is a strong correlation between the thermal sintering of Ir nanoparticles and the OSC of the support.

Figure 2. Correlation of the OSC of the support with the sintering behaviour of supported iridium particles.

We have previously proposed a plausible model to explain the effect of the support on catalyst sintering characteristics [11] summarized briefly below (Fig. 3). The model is further expanded in the context of the present work. An effective electrical double layer, $[\text{O}^{\delta-} - \delta^+](\text{M})$, forms on the catalyst nanoparticle (M) due to lattice oxygen spillover from supports with substantial oxygen ion lability [12, 13]. It should be noted here that the aging protocol followed involves temperatures much greater to the Tamman temperature of IrO_2 , which is ~ 413 °C [19], and is associated with the onset of mobility of metal particles on the surface [20]. Thus small iridium nanoparticle possessing a surface oxide overlayer is expected to be, in principle, highly mobile (therefore prone to sintering) on the surface of all oxide supports investigated in this study, as indeed confirmed experimentally for iridium nanoparticles dispersed on $\gamma\text{-Al}_2\text{O}_3$ [10].

Figure 3. (a) Creation of the effective double layer on Ir particles and its influence on the particles sintering susceptibility through the created electrostatic repulsive forces as well as through the inhibition of the Ostwald Ripening mechanism, (b) labile lattice oxygen acts as a trap for diffusing atomic Ir species.

However, the effective double layer $[\text{O}^{\delta-} - \delta^+]$, created on supports with high oxygen ions lability (Fig. 3a), endows the particle with a net negative charge at its gas-exposed surface, leading to inter-particle repulsion at short range, thus preventing particle-particle encounters followed by coalescence. Such spillover effects are expected to be strongest for supports with the highest oxygen ion lability. In the present case this effect could operate with both metallic Ir^0 and IrO_2 nanoparticles or composites of the two, since IrO_2 is an electronic conductor. In the case of very small Ir particles, labile lattice oxygen creates vacancies that act as traps which inhibit diffusion and agglomeration (Fig. 3b) under a concept consistent to that described in [21, 22]. It is also expected that the $\text{O}^{\delta-}$ modified surface

barrier increases the activation energies for detachment (diffusion) and re-attached of the entities whose transport would otherwise lead to continuous growth of large particles at the expense of smaller particles according to the Ostwald Ripening model (see Fig. 3). All aforementioned effects will be negligible for low-lability supports (e.g. Al₂O₃ and YSZ), which therefore do not prevent particles agglomeration whatever the sintering mechanism is (large particles diffusion and coalescence or Ostwald Ripening). It is worth noting that pure CeO₂ has limited lattice defects concentration in comparison to Gd₂O₃ or ZrO₂-doped CeO₂. Therefore the model suggests that optimal supports against sintering are those with sufficiently high O²⁻ ions mobility i.e. CeO₂ modified with cations such as gadolinium, zirconium and others, that enhance ceria lattice defects, increasing O²⁻ vacancies and consequently O²⁻ mobility [16, 18].

3.2 N₂O decomposition

Figure 4a shows the *light-off* behaviour of all fresh catalysts (Ir/ γ -Al₂O₃, Ir/YSZ, Ir/ACZ and Ir/GDC). N₂O conversion profiles correspond to Ir-free supporting materials are not included in the figure; in accord to literature γ -Al₂O₃, CeO₂ and modified CeO₂ oxide supports similar to that of the present study are almost inactive in direct N₂O decomposition (N₂O conversions <10%) at the temperature range under investigation (300-550°C) [23, 24], whilst Ir is one of the most active catalysts for N₂O decomposition from the Pt-group metals family [9]. Starting with a pre-reduced catalyst a *significant counter-clockwise hysteresis* during heating-cooling is clear for all samples. Holding the sample at maximum temperature until a true steady state was reached caused the system to follow a higher activity, and subsequently reproducible, curve upon cooling (Fig. 4a). This hysteresis indicates changes in the catalyst state, further demonstrated in Figure 4b, which depicts the time-on-stream stability of all fresh and aged catalysts at 450°C. Starting with pre-reduced catalysts, in every case N₂O conversion increased progressively with time-on-stream, stabilizing at maximum activity after ~5-7 h (for Ir/ γ -Al₂O₃ and Ir/YSZ) and ~10-12 h (for Ir/GDC and Ir/ACZ). Since at ~450°C particle growth is not favoured [10], the increase in catalytic activity may be attributed to progressive oxidation of the initially metallic particles under the mildly oxidizing conditions (1000 ppm N₂O), leading to formation of IrO₂ or a superficial overlayer of IrO₂, likely the catalytically active phase, as proposed by Ohnishi et al. [14].

Figure 4. (a) The *light-off* behavior of the fresh Ir/ γ -Al₂O₃, Ir/YSZ, Ir/ACZ and Ir/GDC catalysts showing *counter-clockwise* hysteresis. (b) Time-on-stream stability of all fresh and aged catalysts starting with pre-reduced samples. Other conditions: catalyst mass, $w_{\text{cat}}=50$ mg; total inlet flow rate, $F_t=150$ cm³min⁻¹; N₂O concentration, 1000 ppm(v) N₂O/He.

To avoid pseudo steady-state, all subsequent catalytic measurements for both differential and integral modes of reactor operation were carried out on catalysts that had been stabilized after sufficient time-on-stream. Table 4 lists the temperatures for 20, 50 and 80% conversion (T_{20} , T_{50} and T_{80} , respectively) by the four catalyst pairs, obtained from the corresponding steady state *light-off* profiles. Note that T_{50} values of aged samples are close to those of fresh samples; and unexpectedly in the case of Ir/ γ -Al₂O₃ the T_{50} value of the aged sample is *lower* than that of the fresh sample—i.e. aged Ir/ γ -Al₂O₃ was more active than its fresh counterpart. As we shall see, this behaviour can be rationalized by taking account of the significant particle size dependence of the intrinsic turnover activity of Ir-catalysed N₂O decomposition.

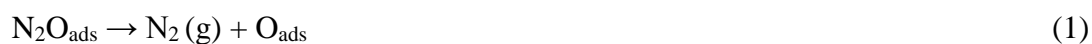
Note also that the activities of the fresh catalysts, which have quite similar particle sizes, are in the order Ir/ γ -Al₂O₃>Ir/YSZ>Ir/GDC>Ir/ACZ, as judged by their T_{50} values (Table 4). This sequence is almost the exact opposite to the OSC sequence of the supports (γ -Al₂O₃ < YSZ < ACZ < GDC) pointing to the presence of metal-support interactions: the higher the oxygen ion lability of the support the higher the inhibition of the de-N₂O activity of the catalyst. In passing, we note that the inverted order between GDC and ACZ is understandable, because although ACZ has lower oxygen storage capacity than GDC, its redox properties are activated at significantly lower temperature (300°C versus 500°C; Table 1). Accordingly, in the temperature interval 350-550°C, within which the N₂O decomposition reaction was investigated, the oxygen lability of ACZ actually exceeds that of GDC. In passing, we note that in the temperature range used all the supports were essentially inactive towards N₂O decomposition. In accord with this, there was no correlation between the BET areas and catalyst activity.

Table 4. T_{20} , T_{50} , T_{80} and TOF values for fresh and aged catalysts at 420°C

Catalyst	$T_{20}/T_{50}/T_{80}$ (°C)		TOF (s ⁻¹)		TOF _{aged} /TOF _{fresh}
	Fresh cat.	Aged cat.	Fresh cat.	Aged cat.	

Ir/ γ -Al ₂ O ₃	394/417/442	378/407/441	3.6×10^{-2}	173×10^{-2}	48.0
Ir/YSZ	408/435/465	422/453/483	5.1×10^{-2}	35×10^{-2}	6.9
Ir/GDC	427/490/>575	437/490/>575	3.5×10^{-2}	1.8×10^{-2}	0.5
Ir/ACZ	466/515/>575	464/522/>575	0.85×10^{-2}	0.56×10^{-2}	0.7

Differential reactor operation (<15% N₂O conversion) at 420°C provided turnover frequency (TOF) values for the fresh and aged catalysts as shown in Table 4. Striking differences between the low and high oxygen ion lability supports is obvious (Table 4). In particular, aged Ir/ γ -Al₂O₃ exhibits a much higher TOF than its fresh counterpart (ca. 48 times higher). TOF_{aged}/TOF_{fresh} is also substantial for Ir/YSZ (~7), whereas only small differences were observed for the Ir/GDC and Ir/ACZ catalyst pairs. This is consistent with the aforementioned sintering behaviour of the catalysts and the known particle size dependence of Ir catalysts in N₂O decomposition: large particles are more active than small ones [14] as we also find here (Table 4). This is also consistent with the view that the influence of the particle size on the de-N₂O activity of Ir-based catalysts is far more important than effects due to metal-support interactions. This is apparent from comparison of the TOF_{aged}/TOF_{fresh} ratio values of Ir/ γ -Al₂O₃ and Ir/YSZ with that of Ir/GDC and Ir/ACZ, suggesting that the O^{δ-} layer created on catalyst particles interfaced with intermediate or high oxygen ion lability supports acts to inhibit de-N₂O activity. According to Vayenas [12] this effective O^{δ-} layer (Fig. 3) is expected to weaken the chemisorption bond of electron acceptor adsorbates such as N₂O_{ads}, and O_{ads} arising from N₂O dissociation. To a first approximation, weakening the chemisorption bonds of both N₂O_{ads} and O_{ads} should have opposite effects on the reaction rate in terms of the well-established mechanism for N₂O dissociation over noble metals:



Weakening both the N₂O_{ads} and O_{ads} chemisorption bonds by oxygen spillover should inhibit reaction (1) whilst also promoting reaction (2). In the present case, the first effect predominates.

4. CONCLUSIONS

Ir nanoparticles on a variety of supports show thermal sintering characteristics that are very strongly correlated with the lability of lattice oxygen in the supporting oxide material: the higher the lability

of oxygen in the support, the lower the vulnerability of the nanoparticles to sintering under oxidative conditions. Oxygen back-spillover from the support to iridium particles causes this resistance to sintering. The same species are responsible for the appearance of metal-support interactions, which cause inhibiting effects on the de-N₂O activity of the iridium particles. These effects are however of significantly less importance than particle size effects on the structure sensitive de-N₂O reaction. The catalytically active phase in direct N₂O decomposition by Ir-based catalysts is IrO₂ or a superficial overlayer of IrO₂.

Acknowledgements IVY acknowledges Technical University of Crete for partial financial support. MJT acknowledges Aston University for a PhD scholarship. GK acknowledges funding from the Royal Society and EPSRC. The authors would like to thank Dr C.M.A. Parlett and Dr M.A. Isaacs for their kind assistance with the TEM measurements.

References

1. Ravishankara AR, Daniel JS, Portmann RW (2009) *Science* 326:123
2. Li L, Xu J, Hu J, Han J (2014) *Environ Sci Technol* 48:5290
3. Centi G, Perathoner S, Vazzana F, Marella M, Tomaselli M, Mantegazza M (2000) *Adv Environ Res* 4:325
4. Liu Z, He F, Ma L, Peng S (2016) *Catal Serv Asia* 20:121
5. Tolman WB (2010) *Angew Chem Int Ed* 49:1018
6. Kapteijn FJ, Rodriguez-Mirasol JA, Moulijn JA (1996) *Appl Catal B* 9:25
7. Li Y, Armor JN (1992) *Appl Catal B* 1:L21
8. Russo N, Mescia D, Fino D, Saracco G, Specchia V (2007) *Ind Eng Chem Res* 46:4226
9. Pachatouridou E, Papista E, Iliopoulou EF, Delimitis A, Goula G, Yentekakis IV, Marnellos GE, Konsolakis M (2015) *J Envir Chem Eng* 3:815
10. Fiedorow RMJ, Chahar BS, Wanke SE (1978) *J Catal* 51:193
11. Yentekakis IV, Goula G, Panagiotopoulou P, Kampouri S, Taylor MJ, Kyriakou G, Lambert RM (2016) *Appl Catal B* 192:357
12. Vagenas CG (2013) *Catal Lett* 143: 1085
13. Vernoux P, Lizarraga L, Tsampas MN, Sapountzi FM, De Lucas-Consuegra A, Valverde J-L, Souentie S, Vayenas CG, Tsiplakides D, Balomenou S, Baranova EA (2013) *Chem Rev* 113:8192
14. Ohnishi C, Iwamoto S, Inoue M (2008) *Chem Eng Sci* 63:5076
15. Duprez D, Descorme C, Birchem T, Rohart E (2001) *Top Catal* 16/17:49
16. Ivanova AS (2009) *Kinet Catal* 50:797
17. Damyanova S, Bueno JMC (2003) *Appl Catal A* 253:135

18. Montini T, Melchionna M, Monai M, Foriasiero P (2016) *Chem Rev* 116:5987
19. Shi H, Li X, Haller GL, Gutierrez OY, Lercher JA (2012) *J Catal* 295:133
20. Hansen TW, Delariva AT, Challa SR, Datye AK (2013) *Accounts Chem Res* 46:1720
21. Hatanaka M, Takahashi N, Tanabe T, Nagai Y, Dohmae K, Aoki Y, Yoshida T, Shinjoh H (2010) *Appl Catal B* 99:336.
22. Dvorak F, Camellone MF, Tovt A, Tran N-D, Negreiros FR, Vorokhta M, Skala T, Matolinova I, Myslivecek J, Matolin V, Fabris S (2016) *Nature Comm* 7:10801
23. Parres-Esclapez S, Illan-Gomez MJ, Salinas-Martinez de Lecea C, Bueno-Lopez A (2010) *Appl Catal B* 96:370
24. Esteves P, Wu Y, Dujardin C, Dongare MK, Granger P (2011) *Catal Today* 176:453